Electronic structure and thermoelectric properties of *n*- and *p*-type SnSe from first-principles calculations

K. Kutorasinski,* B. Wiendlocha, S. Kaprzyk, and J. Tobola

Faculty of Physics and Applied Computer Science, AGH University of Science and Technology, Aleja Mickiewicza 30, 30-059 Krakow, Poland

(Received 16 February 2015; revised manuscript received 20 April 2015; published 7 May 2015)

We present results of the electronic band structure, Fermi surface, and electron transport property calculations in the orthorhombic *n*- and *p*-type SnSe, applying the Korringa-Kohn-Rostoker method and the Boltzmann transport approach. The analysis accounted for the temperature effect on crystallographic parameters in *Pnma* structure as well as the phase transition to *CmCm* structure at $T_c \sim 807$ K. Remarkable modifications of the conduction and valence bands were noticed upon varying crystallographic parameters within the structure before T_c, while the phase transition mostly leads to the jump in the band-gap value. The diagonal components of the kinetic parameter tensors (velocity, effective mass) and resulting transport quantity tensors [electrical conductivity σ, thermopower S, and power factor (PF)] were computed for a wide range of temperature (15–900 K) and hole (*p*-type) and electron (*n*-type) concentrations (10^{17}–10^{21} cm^{-3}). SnSe is shown to have a strong anisotropy of the electron transport properties for both types of charge conductivity, as expected for the layered structure, with the generally heavier *p*-type effective masses compared to *n*-type ones. Interestingly, *p*-type SnSe has strongly nonparabolic dispersion relations, with the "pudding-mold-like" shape of the highest valence band. The analysis of σ, S, and PF tensors indicates that the interlayer electron transport is beneficial for thermoelectric performance in *n*-type SnSe, while this direction is blocked in *p*-type SnSe, where in-plane transport is preferred. Our results predict that *n*-type SnSe is potentially even better thermoelectric material than *p*-type SnSe. Theoretical results are compared with the single-crystal *p*-SnSe measurements, and good agreement is found below 600 K. The discrepancy between the computational and experimental data, appearing at higher temperatures, can be explained assuming an increase of the hole concentration versus T, which is correlated with the experimental Hall data.

DOI: 10.1103/PhysRevB.91.205201 PACS number(s): 71.10.−w, 71.18.+y, 71.20.−b, 84.60.Rb

I. INTRODUCTION

Thermoelectric (TE) conversion in crystalline solids constantly attracts the interest of scientists, not only due to the increasing performance of energy-harvesting systems but also due to the fact that the conventional and "well-known" thermoelectric materials, such as PbX (X = S, Se, Te) [1–3] and Bi_2Te_3 (e.g., [4]), still surprise scientists with their novel and remarkable physical behaviors. It is commonly accepted that TE figure of merit $zT = \sigma S^2/\kappa T$ captures well the basic transport properties of the material at a given temperature T, i.e., electrical conductivity σ, Seebeck coefficient S, and thermal conductivity κ, and is conveniently expressed in dimensionless units. As all these transport quantities apparently depend on temperature and carrier concentration (*n* or *p*), the maximum of zT is expected when properly correlating both intrinsic electron transport properties of the system (e.g., the band-gap magnitude) with temperature range and doping level with the hole or electron concentration to achieve *p*- and *n*-type materials, respectively. However, getting better insight into atomic-level connections among crystal stability, electronic, and lattice properties of TE systems generally allows for a more convincing interpretation of the complex transport phenomena.

Recent experimental work [5] reported $zT \sim 2.6$ at $T \sim 920$ K along one of the axes in single-crystal *p*-type SnSe, which classified this well-known semiconductor as a very promising TE material. However, further results [6,7] revealed much lower zT for polycrystalline samples, showing that SnSe is a rather complex system.

SnSe is a layered material, with an orthorhombic symmetry of the unit cell, and its crystal structure strongly depends on temperature. First of all, SnSe exhibits a crystallographic phase transition at $T_c = 807$ K [8]. Below T_c, its unit cell can be described in *Pnma* simple orthorhombic space group 62, with four chemical formulas (eight atoms) in the unit cell (see Fig. 1). Crystal structure parameters of this "low-temperature" (i.e., below T_c) phase depend on temperature as well [8]. Since the temperature dependence of the transport properties (e.g., thermopower) is discussed in our work, those changes in crystal structure were also taken into account. Accordingly, three cases are considered: a low-temperature (LT) phase, described by the experimental crystallographic data taken at $T_{expt} = 295$ K and used in our calculations to represent SnSe in the temperature range $T_{calc} = 10$–550 K; a middle-temperature (MT) phase ($T_{expt} = 790$ K and $T_{calc} = 550$–807 K); and high-temperature (HT) phase ($T_{expt} = 829$ K and $T_{calc} > 807$ K), as displayed in the Table I. Above T_c, the high-temperature phase has an orthorhombic *c*-base-centered *CmCm* space group (No. 63). The transition from the simple to the centered unit cell reduces the number of atoms in the primitive cell from eight to four, changing the shape and size of the Brillouin zone (BZ). Thus, it becomes impossible to directly compare the electronic dispersion relations between the LT/MT and HT phases when using the HT centered unit cell. Therefore, to allow for a better understanding and easier analysis of the role of the phase transition in the evolution of the electronic structure and transport properties of SnSe, we transformed the HT SnSe centered unit cell into the equivalent *Pbmm*

*kamil.kutorasinski@fis.agh.edu.pl

 ©2015 American Physical Society

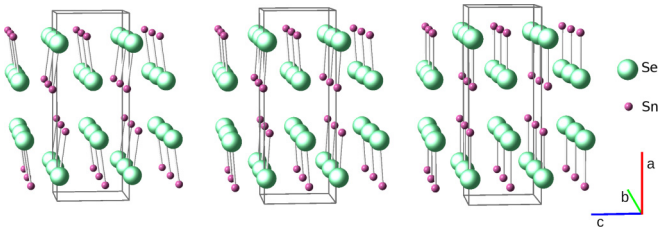

FIG. 1. (Color online) Crystal structure of SnSe (Se, large green balls; Sn, small magenta balls). (left) LT phase (*Pnma* at 295 K), (middle) MT phase (*Pnma* at 790 K), and (right) HT phase (*Pbmm* above 807 K).

simple orthorhombic one (No. 51). The *Pbmm* unit cell has the same number of atoms as and an alignment of the unit cell axes similar to the structure before the transition (i.e., a axis is the longest, b is the shortest, and c is in between; see Fig. 1). With this transformation, the Brillouin zone and the location of the high-symmetry points remain similar in both phases (small changes are only in BZ dimensions due to lattice parameters' variation). In our computations, the actual values of the lattice parameters for the HT phase were taken from the high-temperature ($T = 829$ K) neutron measurements [8] and are shown in Table I. It is worth noting that the crystal structure of SnSe evolves smoothly with temperature (even while crossing T_c) and the unit cell dimensions, as well as interatomic distances, change rather continuously with temperature (see Table I and Ref. [8]). The crystal structure parameter, which exhibits the most rapid change at T_c, is the z parameter positioning Sn and Se atoms.

Recently, first-principles calculations of transport properties of p-type SnSe were reported in Ref. [9]. In our work we give a more extended analysis of the electronic structure, effective masses, and transport properties of both n- and p-type SnSe. The constant relaxation time approximation is used, and phonon drag effects are not discussed.

This paper is organized as follows. In Sec. II theoretical and computational details are presented. Section III A describes in detail the electronic band structure and the Fermi surface of the valence and conduction states, together with the effective mass and the transport function analysis. Section III B discusses anisotropic (single-crystal) and isotropic (polycrystalline-like) transport properties as a function of temperature and carrier concentration, and a comparison with experimental data is carried out. Section IV contains a summary and the conclusions of the work. In Appendix A, formulas for averaging the anisotropic transport coefficients are derived in order to compute their isotropic (polycrystalline) analogs. Appendix B contains complementary data.

TABLE I. Crystallographic data [8] for the SnSe compound, measured at different temperatures T_{expt}, used in our calculations for selected temperature ranges T_{calc}.

Phase	T range	Space group	Lattice constant (Å)	Atomic positions	Sn	Se
LT	$T_{\text{expt}} = 295$ K	*Pnma*	$a = 11.501$	x:	0.6186	0.3551
	$T_{\text{calc}} < 550$ K	No. 62	$b = 4.153$	y:	0.25	0.25
			$c = 4.445$	z:	0.1032	0.4818
MT	$T_{\text{expt}} = 790$ K	*Pnma*	$a = 11.620$	x:	0.6230	0.3553
	$T_{\text{calc}} = 550$–807 K	No. 62	$b = 4.282$	y:	0.25	0.25
			$c = 4.334$	z:	0.0584	0.4878
HT	$T_{\text{expt}} = 829$ K	*Pbmm*[a]	$a = 11.62$	x:	0.6248	0.3558
	$T_{\text{calc}} > 807$ K	No. 51[a]	$b = 4.282$	y:	0.25	0.25
			$c = 4.293$	z:	0.00	0.50

[a]Transformed from *CmCm* (No. 61)

II. THEORETICAL DETAILS

A. Thermopower

The Boltzmann transport theory [10–12], which has successfully been applied to study transport properties of various crystalline materials [13–15], is used to calculate the energy-dependent electrical conductivity $\boldsymbol{\sigma}(\mathscr{E})$ (so-called transport function, TF):

$$\boldsymbol{\sigma}(\mathscr{E}) = e^2 \sum_n \int \frac{d\mathbf{k}}{4\pi^3} \tau_n(\mathbf{k}) \mathbf{v}_n(\mathbf{k}) \otimes \mathbf{v}_n(\mathbf{k}) \delta[\mathscr{E} - \mathscr{E}_n(\mathbf{k})]. \quad (1)$$

The symbol $\otimes$ represents the outer product (Kronecker product) of two vectors, $\mathbf{v}_n(\mathbf{k}) = \nabla_k \mathscr{E}_n(\mathbf{k})$, and $\tau_n(\mathbf{k})$ is the velocity and lifetime of electrons on band $\mathscr{E}_n(\mathbf{k})$. The transport function tensor has to be reformulated into a form that is more convenient for the numerical computation. With the use of the constant relaxation time approximation [$\tau_n(\mathbf{k}) = \tau_0$] and after changing the three-dimensional $\mathbf{k}$-space integration to the two-dimensional surface integration [$\mathscr{E}_n(\mathbf{k}) \rightarrow S_n(\mathscr{E})$], it takes the form

$$\boldsymbol{\sigma}_\tau(\mathscr{E}) = \tau_0 \frac{e^2}{\hbar} \sum_n \int_{S_n(\mathscr{E})} \frac{dS}{4\pi^3} \frac{\mathbf{v}(S_n(\mathscr{E})) \otimes \mathbf{v}(S_n(\mathscr{E}))}{|\mathbf{v}(S_n(\mathscr{E}))|}. \quad (2)$$

TF is directly related to the macroscopic transport coefficients, such as thermopower, the electronic part of thermal conductivity, and electrical conductivity. Within this approach [10] the two basic transport tensors (electrical conductivity $\boldsymbol{\sigma}_e$ and thermopower $\boldsymbol{S}$) can be expressed as

$$\boldsymbol{\sigma}_e = \mathscr{L}^{(0)}, \quad \boldsymbol{S} = -\frac{1}{eT} \frac{\mathscr{L}^{(1)}}{\mathscr{L}^{(0)}}, \quad (3)$$

where

$$\mathscr{L}^{(\alpha)} = \int d\mathscr{E} \left(-\frac{\partial f}{\partial \mathscr{E}} \right) (\mathscr{E} - \mu_c)^\alpha \boldsymbol{\sigma}(\mathscr{E}). \quad (4)$$

The value of the chemical potential $\mu_c = \mu_c(T, n_d)$ depends on the temperature T, the carrier concentration, and the type of conductivity (n, p; see Sec. II C).

In the case of an anisotropic structure, such as orthorhombic SnSe, the transport function tensor (and thermopower as well) has three linearly independent elements, and in this work, diagonal elements (i.e., S_{xx}, S_{yy}, S_{zz}) are calculated. For the polycrystalline sample without texture, those three elements have to be averaged in the proper way to obtain the macroscopically isotropic thermopower and power factor (PF). The relevant formulas are given here and are derived in

Appendix A:

$$S_{\text{avg}} = \frac{S_{xx}\sigma_{xx} + S_{yy}\sigma_{yy} + S_{zz}\sigma_{zz}}{\sigma_{xx} + \sigma_{yy} + \sigma_{zz}}, \tag{5}$$

$$\text{PF}_{\text{avg}} = \frac{1}{3}\left(S_{xx}^2\sigma_{xx} + S_{yy}^2\sigma_{yy} + S_{zz}^2\sigma_{zz}\right). \tag{6}$$

Since the power factor, in the constant-relaxation-time approximation, depends linearly on the relaxation time τ (not calculated here), PF divided by τ is presented.

B. Density of states and effective mass

In a way similar to that for the transport function, the density of states (DOS) is calculated:

$$g(\mathscr{E}) = \sum_n \int_{S_n(\mathscr{E})} \frac{dS}{4\pi^3} \frac{1}{|\nabla_k \mathscr{E}_n(\mathbf{k})|}. \tag{7}$$

With this definition $g(\mathscr{E})$ has units of eV^{-1} m^{-3}; that is, it includes the volume of the unit cell.

The DOS function is closely connected to the DOS effective mass m^*. Here, energy-dependent m^* is calculated using the formula [15]

$$m_{\text{DOS}}(\mathscr{E}) = m_e m^*_{\text{DOS}}(\mathscr{E}) = \hbar^2 \sqrt[3]{\pi^4 g(\mathscr{E}) g'(\mathscr{E})}. \tag{8}$$

Alternatively, effective mass can be computed by integrating the effective mass tensor over the isoenergetic surfaces:

$$m_{ij}(\mathscr{E}) = m_e m^*_{ij}(\mathscr{E}) = \int_{S_n(\mathscr{E})} [\boldsymbol{M}_{ij}] dS \Big/ \int_{S_n(\mathscr{E})} dS, \tag{9}$$

where the effective mass tensor is defined as [10]

$$[\boldsymbol{M}_{ij}]^{-1} = \frac{1}{\hbar^2} \frac{\partial^2 \mathscr{E}}{\partial k_i \partial k_j}. \tag{10}$$

Using Eqs. (9) and (10), one may discuss the direction dependence of the effective mass. In the case of an orthorhombic structure with orthogonal axes, the $[\boldsymbol{M}_{ij}]$ tensor is diagonal, and components m^*_{xx}, m^*_{yy}, and m^*_{zz} are computed.

The isotropic band effective mass is determined by the geometrical mean

$$m^*_{iso} = \sqrt[3]{m^*_{xx} m^*_{yy} m^*_{zz}}. \tag{11}$$

Both ways of calculating effective mass [DOS effective mass from Eq. (8) and band effective mass from Eq. (11)] give the same results for only parabolic bands. The difference between those two results gives us an opportunity to estimate the importance of nonparabolicity of the electronic band structure.

The aforementioned effective masses correspond to the $T = 0$ K temperature. The temperature effects can be taken into account via the Fermi-Dirac distribution function in a similar way, as in the thermopower calculation in Eq. (3). The actual number of "active" (conducting) electrons, at temperature T, can be represented as $n_{\text{active}} = \int d\mathscr{E}\, g(\mathscr{E})(-\frac{\partial f}{\partial \mathscr{E}})$, and the effective mass of active electrons as a function of temperature can be determined from

$$m^*(T, n_d) = \frac{\int d\mathscr{E}\, m^*(\mathscr{E}) g(\mathscr{E}) \left(-\frac{\partial f}{\partial \mathscr{E}}\right)}{\int d\mathscr{E}\, g(\mathscr{E}) \left(-\frac{\partial f}{\partial \mathscr{E}}\right)}, \tag{12}$$

where n_d is the carrier concentration at which m^* is calculated (see Sec. II C). Note that this analysis requires an assumption that effective mass is well defined, which for strongly nonparabolic bands may not be valid.

C. Doping and chemical potential

SnSe is an intrinsic semiconductor, where the Fermi energy lies inside the gap. As already mentioned, the transport properties of the intrinsically (defect-doped) p-type single-crystal [5], polycrystal [6], and p-type Ag-doped polycrystal [7] samples have already been reported. To simulate the behavior of the system after doping, we use the rigid-band model [16]. In this approach, an additional number n_d of electrons or holes is the control parameter, added to mimic n-type (positive n_d) or p-type (negative n_d) behavior, and the chemical potential $\mu_c = \mu_c(T, n_d)$ needed in Eq. (4) is calculated using the formula

$$n + n_d = \int d\mathscr{E}\, g(\mathscr{E}) \frac{1}{1 + \exp\left(\frac{\mathscr{E} - \mu_c(T, n_d)}{k_B T}\right)}. \tag{13}$$

Here n is the total number of valence electrons in the system (which is 10/f.u. in the case of SnSe), and the integral is taken from the bottom of the valence bands.

D. Band structure computational details

Electronic band structure calculations were performed using the full-potential Korringa-Kohn-Rostoker [17–22] (KKR) method, within the scalar relativistic approach [23,24]. The local-density-approximation (LDA) parametrization of Perdew and Wang [25] was employed. The self-consistent cycle was repeated until the difference between the input and output potentials was less than 1 mRy at any point inside the unit cell. Isoenergetic surfaces $S_n(\mathscr{E})$ were obtained with the use of the marching cube algorithm [26] on a mesh consisting of $80 \times 80 \times 80$ voxels. To improve visualization, vertex normal [27] and vertex color techniques were also used. All energy-dependent functions were calculated with a resolution of 2.5 meV. The transport function was additionally interpolated between energy mesh points, using spline functions, which allows us to obtain converged results for temperatures above 10 K in the concentration range of 10^{17}–10^{21} cm^{-3}.

III. RESULTS

A. Electronic structure

Electronic dispersion relations are shown in Fig. 2 for the LT [Fig. 2(a)], MT [Fig. 2(b)], and HT [Fig. 2(c)] phases [28] of SnSe. As expected, the LDA, used in this work, underestimated the band gaps. Since the gap value is the important parameter in transport property calculations, especially at elevated temperatures, the computed band gaps were expanded to mimic the experimental ones (see Table II). For the LT phase, the band-gap value was set to $E_g^{\text{exp}} = 0.86$ eV [5]. In the MT and HT phases, for which experimental data are not available, the calculated gap values were extrapolated proportionally to those in the LT phase; that is, we assume that the LDA underestimation is proportional to the real gap value. It is worth noting that the calculated values of the energy gaps

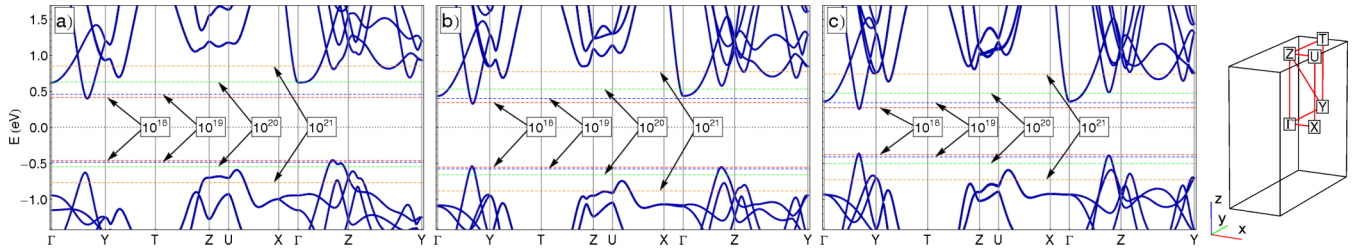

FIG. 2. (Color online) Electronic band structure of the (a) LT, (b) MT, and (c) HT phases of SnSe, computed along the high-symmetry directions, as shown in the orthorhombic Brillouin zone. Horizontal lines mark the Fermi energy positions (μ_c at $T = 0$ K) for electron/hole concentrations (in cm^{-3}) of $n = 10^{18}$ (red), $n = 10^{19}$ (blue), $n = 10^{20}$ (green), and $n = 10^{21}$ (orange).

for the LT and MT phases are almost the same, whereas the HT phase has a much smaller gap (see Table II). To verify whether the reduction of the band gap is related to the change in atomic positions or the unit-cell parameters, additional calculations were performed for the MT phase, using (i) the MT atomic parameters and HT lattice constants and (ii) MT lattice constants and HT atomic parameters. The resulting LDA band gaps were 0.465 and 0.355 eV, respectively; thus, we found that the gap value is controlled mainly by the Sn and Se atomic positions. Recent calculations [9], using the GW method, reported $E_g = 0.829$ eV for the LT phase and 0.46 eV for HT; thus, a reduction of E_g after the phase transition was also found.

As we explained in the Introduction, due to the transformation of the HT crystal structure to the simple orthorhombic *Pbmm* space group, Brillouin zones in all (LT, MT, and HT) phases in our calculations have the same shape and high-symmetry points (BZ is shown schematically in Fig. 2). The reciprocal-space x,y,z axes are parallel to the a,b,c real-space directions. Let us start with some general comments about the band structure before going into a detailed analysis of the effective masses and the transport properties. In the LT phase, the highest valence band (VB) appears in the Γ-Z direction, parallel to the z axis. It is worth noting that in the LT phase, this highest VB has a "pudding-mold-like" shape, which is reported to be beneficial for thermoelectric performance in other systems [29]. For the higher-temperature structures (MT and HT), valence bands are much different, which points out that electronic band structure is sensitive to temperature, as simulated by the unit-cell changes. The pudding mold-like VB changes shape to become more parabolic, and the second VB in the Γ-Y direction aligns with the band in the Γ-Z direction. The lowest conduction band (CB), seen in the Γ-Y direction in all phases, is parabolic-like. Above the band gap we see that the whole band structure in the Γ-Z direction moves down considerably when going from LT to HT, which is correlated with the shortening of the corresponding unit-cell c axis. In the LT structure, the in-plane unit-cell parameters, $b = 4.153$ Å and $c = 4.445$ Å, are significantly different, which in the reciprocal space is reflected by the different alignments of the Γ-Y and Γ-Z bands. After the phase transition, like in the MT case, $b \simeq c$, and the energy locations of CB minima and VB maxima become similar between those two directions. What seems quite surprising is that the differences in the band structures between the LT and MT structures (before the phase transition) are much larger than those between the MT and HT structures (i.e., induced by the phase transition). This shows that the electronic structure evolves continuously with temperature; however, the band gap changes abruptly at the phase transition (see Table II), which can result in rapid changes in the transport properties.

It is also interesting to analyze the bands in the Z-U and Γ-X directions, which represent the real-space a direction, i.e., contribute the charge transport between the SnSe layers. In all cases, for the VB part, the resulting bands are very flat, which is quite intuitive since we expect hampered charge propagation in this direction. On the other hand, the conduction band in the Γ-X direction is very steep and almost linear. All these band structure features are reflected in the transport properties of SnSe, as discussed below.

TABLE II. Calculated (LDA) and experimental [5] values of the energy band gap (in eV) in SnSe for the three structures, LT, MT, and HT. The last column shows the extrapolated values, used in transport calculations (see, text).

Structure	LDA	Experiment	Used in calculations
LT	0.474	0.86	0.86
MT	0.487	no data	0.87
HT	0.350	no data	0.64

1. *n-Type doping*

For n-type doping (whatever the LT, MT, and HT structures) at electron concentrations $<10^{19}$ cm^{-3}, the Fermi level reaches one ellipsoidal electron pocket (with twofold degeneracy) in the Γ-Y direction [see Figs. 2 and 3(a)–3(c)]. The band forming this pocket has a regular, parabolic-like shape, and isotropic effective mass is $m^*_{iso} \simeq 0.3$–0.4 in the LT case and $m^*_{iso} \simeq 0.2$–0.3 in the MT and HT cases. The highest values of m^* are found along the x direction [see Figs. 4(b), 4(d), and 4(f)], where they quickly exceed $m^*_{xx} \simeq 0.5$. Therefore, velocity integrated over the Fermi surface (i.e., transport function) is 3 times lower in the x direction than in the y and z directions [see Figs. 5(b), 5(d), and 5(f)], and low x-direction electrical conductivity is expected [since $\sigma_e \sim \sigma(\mathscr{E}_F)$]. This behavior corresponds to our expectations of the lower electrical conductivity perpendicular to SnSe layers (the x direction is along the a axis). Electron transport properties change dramatically when the Fermi level reaches further electron pockets, one in the HT and MT structures at the Γ point at $\sim 10^{19}$ cm^{-3} and five in the LT structure (one centered at

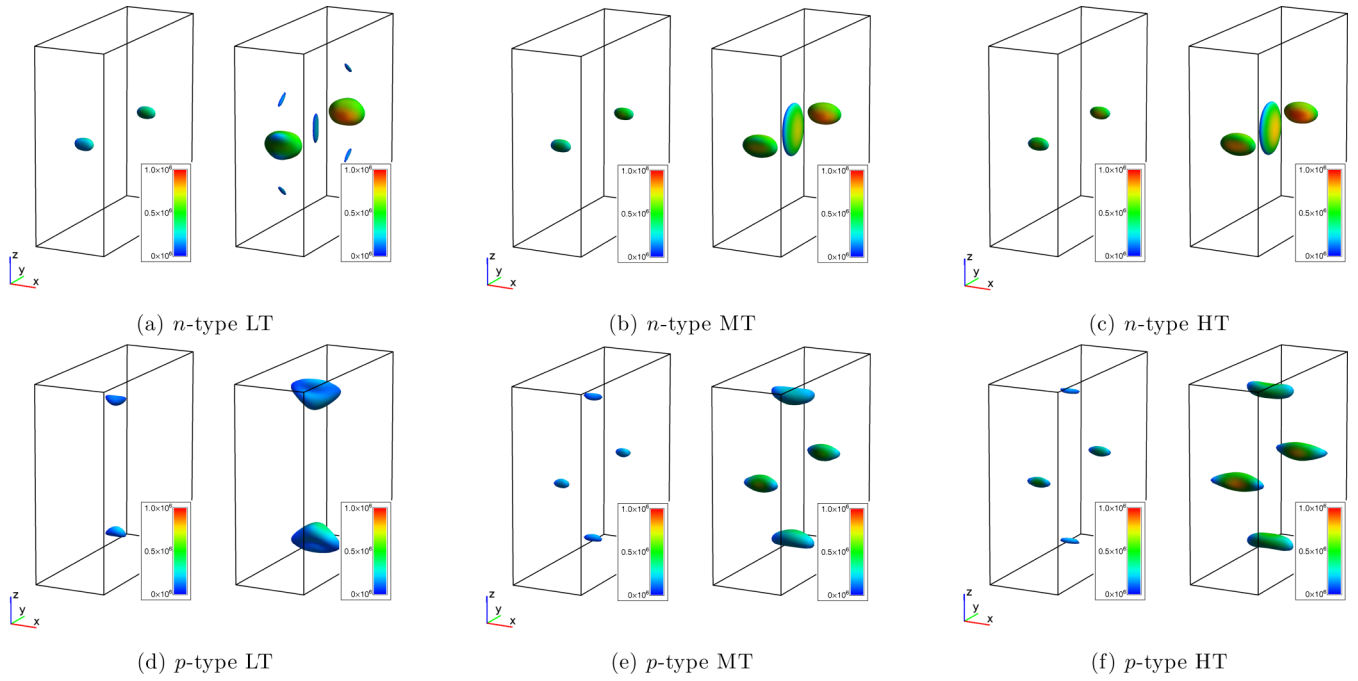

(a) n-type LT (b) n-type MT (c) n-type HT

(d) p-type LT (e) p-type MT (f) p-type HT

FIG. 3. (Color online) Fermi surfaces of the (left) LT, (middle) MT and (right) HT phases of SnSe for the (a)–(c) n-type and (d)–(f) p-type doping for carrier concentrations (in cm^{-3}) of 10^{19} (left subpanel) and 10^{20} (right subpanel). Electron velocities (in m/s) are represented by a color scale.

the Γ point and four in the Γ-T direction) at $\sim 10^{20}$ cm^{-3}. At these concentrations, the aforementioned steep linear band in the Γ-X direction is activated. In contrast to the previous case, these new pockets have the smallest m_{xx} (see Fig. 4), while the largest mass tensor component is now m_{zz}. As a consequence, the average effective mass, represented by m^*_{iso} or m^*_{DOS}, increases rapidly to 1.0–1.5 (for $n \sim 10^{20}$ cm^{-3} in LT) and 0.6–0.9 (for $n \sim 10^{19}$ cm^{-3} in HT and MT). Thus, the transport function tensor component σ_{xx} [Figs. 5(b) and 5(d)] changes from the smallest in the energy range corresponding to the electron concentration below 10^{19} cm^{-3} to the largest at energies corresponding to 10^{20} cm^{-3}. The rapid increase of σ_{xx} (connected to the alignment of the five pockets at the same energy) should favor high thermopower S_{xx} since $S \sim d(\ln \sigma)/d\mathscr{E}$. In the case of n-type doping, in the LT, MT, and HT phases, after a certain concentration is reached between 10^{19} cm^{-3} (HT) and 10^{20} cm^{-3} (LT; see Fig. 5), two types of electrons are involved in the electrical transport along the x direction: first, those with low mass and high velocity, which provide high conductivity, and, second, heavy electrons that are needed to achieve high thermopower. In such a case, a large power factor can be expected.

DOS effective mass, plotted as a function of the carrier concentration and temperature [temperature effects according to Eq. (12)], is shown in Fig. 6. For the sake of completeness, we present results for all the phases (LT, MT, and HT) in the wide 15–900 K temperature range. The appearance of additional electron pockets, which are manifested in the rapid rise of the effective mass, has sharply determined concentrations only at very low temperatures. For $T = 300$ K, due to temperature blurring of the Fermi-Dirac statistics, m^* changes gradually with a pronounced bump above 10^{20} cm^{-3} in the LT structure. At temperatures around $T = 800$ K or higher, electrons, which actively conduct, presumably come from the deeper-lying bands that have strongly nonparabolic dispersion relations. Thus, effective mass is not well defined, and the results must be treated with caution. Generally, in all the phases, DOS effective masses rise with the concentration from approximately $0.3m_e$ at $n = 10^{18}$ cm^{-3} to $2m_e$ to $3m_e$ at $n = 10^{21}$ cm^{-3}.

2. *p-Type doping*

In the p-type LT structure, up to 10^{20} cm^{-3}, the Fermi level penetrates hole pockets located in the Γ-Z direction [Fig. 3(d)]. These pockets have a nonellipsoidal shape, which is caused by the pudding-mold-like band, because they have two maxima [see Fig. 2(a)]. In this case, effective mass cannot be well defined [see Fig. 4(a)] since such a band exhibits both electronlike and holelike properties due to the convex and concave curvatures. However, the Fermi surface shape indicates that the x-direction effective mass possesses the highest value (elongated shape in the x direction), which, in real space, corresponds to the a-axis direction (perpendicular to the SnSe layers). This behavior obviously affects the carrier velocity, integrated over the Fermi surface [see Fig. 5(a)]. The component σ_{xx}, similar to that in the n-type case, is again the lowest and the highest values of TF detected in the z (close to the VB edge) and y directions (well below the VB edge), with both directions being parallel to the SnSe atomic layers. Interestingly, at higher temperatures (MT and HT phases) the bands in the Γ-Z direction do not have inflection, and the effective mass is therefore well defined. At higher concentrations (10^{20}–10^{21} cm^{-3}) in LT, the Fermi level also reaches holes from the Γ-Y direction [see Figs. 2(a) and 3(a)]. In HT (and also MT), the axial anisotropy of the transport properties of SnSe (m^* and TF) is nicely visible: a

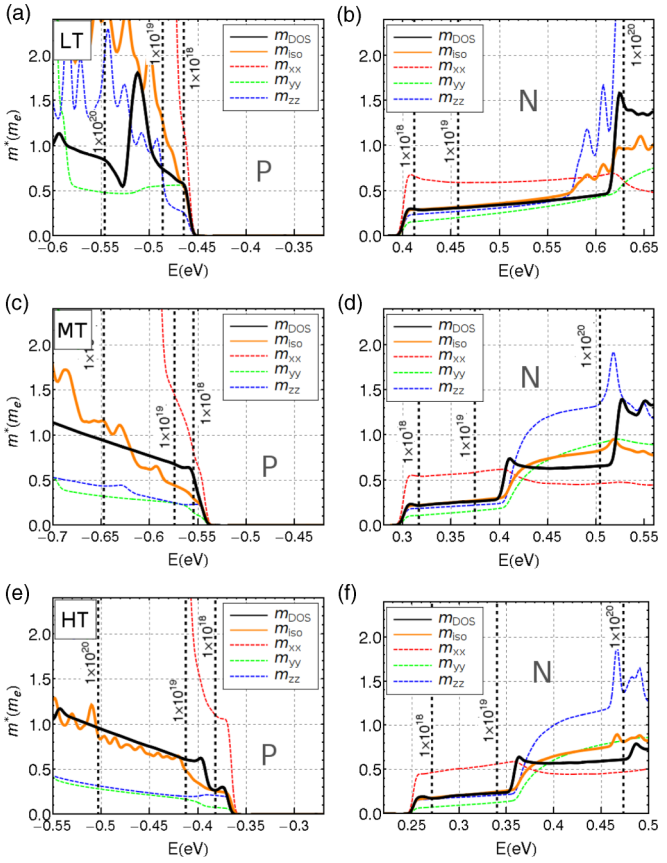

FIG. 4. (Color online) Effective mass of the (a) and (b) LT, (c) and (d) MT, and (e) and (f) HT phases of SnSe, calculated using Eq. (8) (m_{DOS}), Eq. (9) (m_{xx}, m_{yy}, and m_{zz}), and Eq. (11) (m_{iso}). In each case, zero energy is fixed in the middle of the energy gap. Black vertical lines show the Fermi level for various carrier concentrations (in cm^{-3}): 1×10^{18}, 1×10^{19}, and 1×10^{20}. Left and right columns present results for the p-type and n-type doping, respectively.

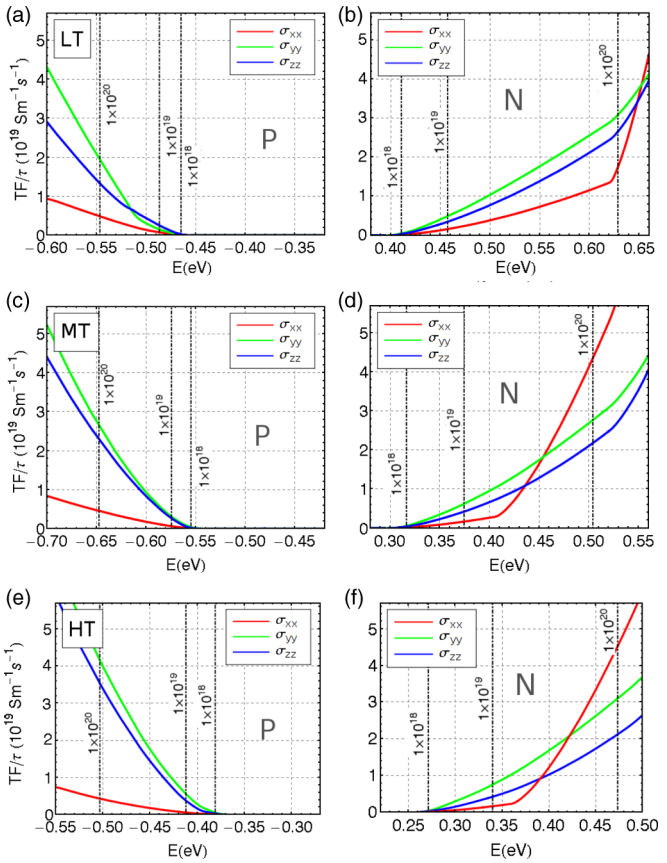

FIG. 5. (Color online) Transport function (TF) of valence and conduction bands in LT, MT, and HT phases of SnSe. Zero energy is fixed in the middle of energy gap, as in Fig. 2. Black vertical lines show the Fermi level for various carrier concentrations (in cm^{-3}): 1×10^{18}, 1×10^{19}, and 1×10^{20}. Left and right columns present results for p-type and n-type doping, respectively.

very large effective mass and the smallest transport function are seen in the x direction, compared with those in the much more "conducting" y and z directions (in-plane transport). The electrical conductivity $\sigma_{e,xx}$ is expected to be about 3 times lower [see Fig. 5(c)] than in the other directions.

Figure 6 (left column) shows p-type DOS effective mass as a function of the carrier concentration and temperature. The LT structure, already at $n = 10^{18}$ cm^{-3}, has a very large value of the "bare" mass (i.e., not affected by temperature blurring, $T = 15$ K curve), $m^* \simeq 1.0$, which increases significantly above $n = 2 \times 10^{19}$ cm^{-3}. At $T = 300$ K, like for the n-type doping, the critical concentration, where additional bands start to influence m^*, is blurred, and m^* is almost constant ($m^* \simeq 1.5$) up to 10^{20} cm^{-3}, then increases to $3m_e$ at $n = 10^{21}$ cm^{-3}. At higher temperatures, the deep and heavy valence bands contribute to the effective mass even at the lowest concentrations; however, we have to keep in mind that the integral in Eq. (12) covers carriers far from the gap, where bands are generally not parabolic; thus, the characterization of bands in terms of the effective mass may become inaccurate.

Closing the effective mass discussion, for all the LT, MT, and HT cases, n-type effective masses are smaller than p-type effective masses.

B. Transport properties

1. *Thermopower*

Thermopower as a function of electron/hole concentration for the three different temperatures is presented in Fig. 7, where data for the different temperatures were obtained for the corresponding crystal structures. The complete results for all the phases at all temperatures are shown in Appendix B. The most interesting features are seen for the n-type LT case, which exhibits strong anisotropy of the Seebeck coefficient, visible at $T = 70$ and 300 K around $n \sim 10^{20}$ cm^{-3}. The n-type S_{xx} tensor element has the largest absolute value; at low temperatures S_{xx} starts to dominate at 1×10^{20} cm^{-3}, where the Fermi energy reaches five electron pockets with high v_x [see red line in Fig. 5(b)]. At higher temperatures (i.e., for MT and HT), around $n \sim 2 \times 10^{19}$ cm^{-3}, E_F reaches only one additional electron pocket [see Figs. 5(d) and 5(f), red line], and the advantage of reaching this pocket spreads over a wider concentration range (see n-type S_{xx} at 807 K in Fig. 7). This is reflected as an ~20% rise in the S_{xx} thermopower in the whole concentrations range.

The anisotropy of p-type thermopower is less significant. An enhancement of the thermopower similar to that observed for the n-type thermopower, caused by the appearance of

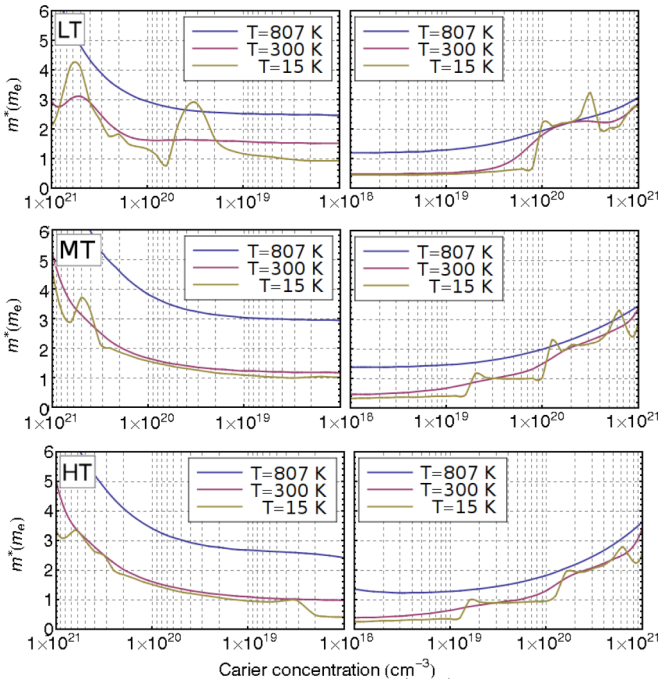

FIG. 6. (Color online) DOS effective mass as a function of the carrier concentration and temperature for the LT, MT, and HT phases of SnSe. Left and right columns correspond to the p-type and n-type doping, respectively.

additional bands near the Fermi level, is seen in the p-type S_{yy} component at $p \approx 3 \times 10^{19}$ cm^{-3}. Two nonparabolic pockets have a high velocity of electrons in the y direction, increasing rapidly at $p \approx 3 \times 10^{19}$ cm^{-3}, which provides the increase in the σ_{yy} derivative [see green line in Fig. 5(a)]. The significance of this effect is smaller than for the n-type doping and is seen only in the LT phase, but it is sufficient to provide an increase in S_{yy} over S_{xx} and S_{zz} (best seen at 300 K).

As far as the bipolar effects are concerned, we can observe that the p-type S_{xx} element shows the strongest reduction at

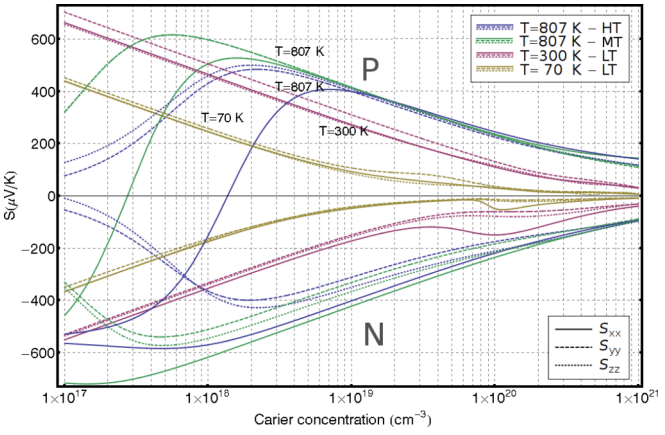

FIG. 7. (Color online) Thermopower as a function of the carrier concentration for the (top) p-type and (bototm) n-type SnSe for T = 70, 300, and 807 K. The electronic band structures of different phases were used to calculate thermopower: LT at 70 and 300 K and MT and HT at 807 K.

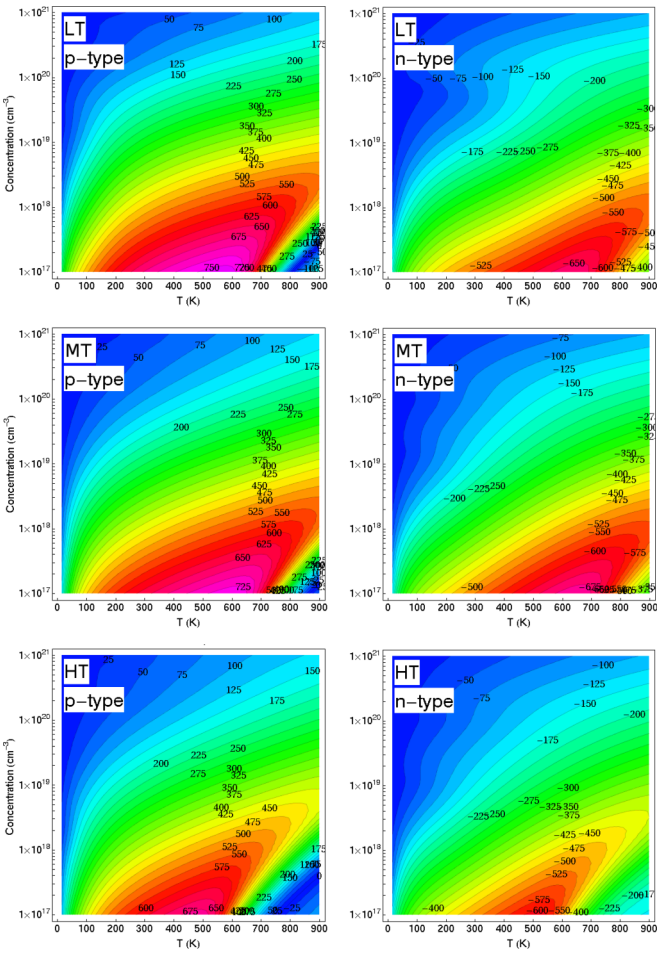

FIG. 8. (Color online) Isotropic thermopower for LT, MT, and HT phases of SnSe (see Table I) for n- and p-type doping.

the high temperature, which is caused by the large n-type S_{xx} and σ_{xx}. The major detrimental effect at high temperatures is related to the reduction of the band gap during the phase transition (LT and MT vs HT; see Table II). To visualize the influence of the gap reduction on the bipolar effect, we have plotted S at the same temperature of 807 K (phase-transition temperature) computed for the MT and HT cases. The much smaller band gap in the HT phase leads to the much stronger bipolar effect, and the thermopower starts to decrease already for $p < 10^{19}$ cm^{-3} and $n < 2 \times 10^{18}$ cm^{-3}. Note also that the bipolar effect critically depends on the value of the band gap, which here for the HT phase was adjusted in an approximate way since we are not aware of the experimental value.

Isotropic thermopower, calculated using Eq. (5), is shown as a color map in Fig. 8, and $S(T)$ curves for selected carrier concentrations are collected in Appendix B (see Fig. 16). To allow for a comparison between the different phases, all three cases for complete temperature ranges are displayed. After averaging over three directions, in all three phases, p-type thermopower is generally larger than n-type thermopower. For the n-type LT map, around $n \sim 10^{20}$ cm^{-3} and below 400 K, we observe the abnormal bending of S, which increases with the carrier concentration. This is due to the rise in the S_{xx} element, as discussed before. For the MT and HT phases, such

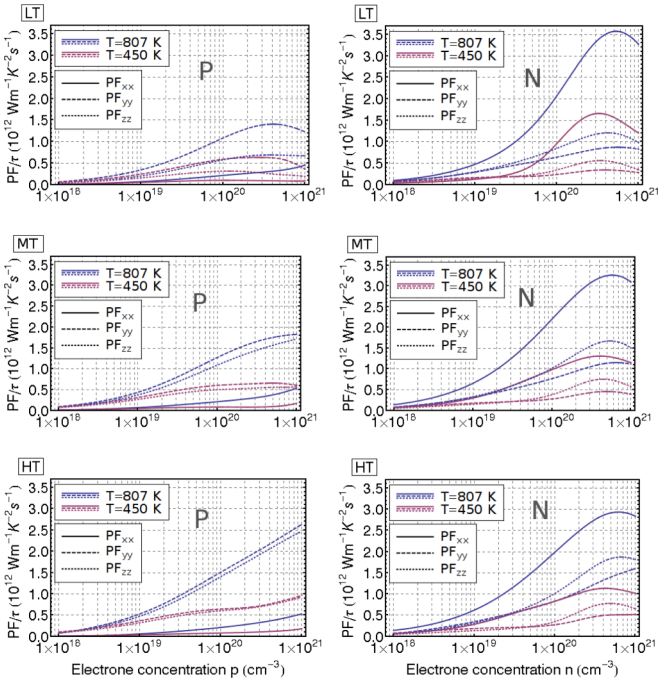

FIG. 9. (Color online) Power factor of the LT, MT, and HT phases for (left) p-type and (right) n-type SnSe as a function of concentration for two temperatures (450 and 807 K), calculated along three directions.

an effect is not observed, and the variation of S with the carrier concentration is monotonic (S decreases with n or p). At the highest temperatures and the lowest carrier concentrations, we again observe a drop in S due to the bipolar effects, which is strongest for the p-type HT phase.

2. *Power factor*

The power factor ($\mathrm{PF} = S^2/\sigma$), similar to the electrical conductivity, cannot be directly calculated if the electronic relaxation time τ is not known; however, the discussion of PF/τ can still be very useful in optimizing the carrier concentration in the SnSe system. For completeness of the analysis, we show results for all the phases (LT, MT, and HT) at $T = 450$ and 807 K, although one has to bear in mind that these phases describe SnSe in limited temperature ranges.

Results of the calculations are shown in Fig. 9. The most striking observation is that for p-type SnSe, the xx tensor element of the power factor PF_{xx} is the smallest one, in contrast to n-type SnSe, where PF_{xx} is the largest. The reason is that in p-type SnSe, the x-direction interlayer conducting channel is blocked due to the smallest TF (see Fig. 5, red line), whereas in n-type SnSe, it is activated by the electron pockets with high v_x. The smallest p-type PF_{xx}, compared with those in the y and z directions, remains in agreement with the experimental findings [5].

In the p-type LT phase, the value of the thermopower is approximately isotropic (except for S_{xx} at low concentrations); thus, overall anisotropy in the PF is due to the electrical conductivity: the transport function element σ_{yy}/τ has the biggest value (in $p > 5 \times 10^{19}$ cm^{-3}), which makes PF largest in the y direction. For the high-temperature structures, namely,

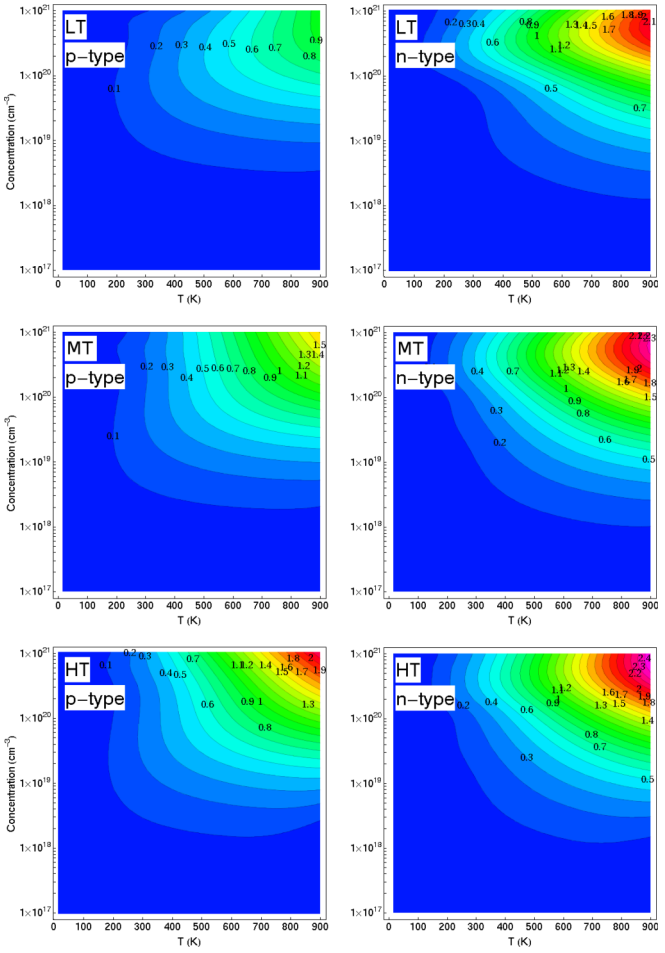

FIG. 10. (Color online) Isotropic power factor for n- and p-type SnSe (LT, MT, and HT phases) as a function of the carrier concentration and temperature. All values are in 10^{12} W K^{-2} m^{-1} s^{-1}.

MT and HT, the power factors for the y and z directions become similar, and PF is largest for the HT phase. In n-type SnSe, PF/τ curves look quite similar when comparing the LT, MT, and HT cases, with decreasing anisotropy (measured as $\mathrm{PF}_{xx}/\mathrm{PF}_{yy}$ and $\mathrm{PF}_{xx}/\mathrm{PF}_{zz}$) upon going from LT to HT.

For isotropic (polycrystalline) material, the power factor, calculated using Eq. (6), is mapped in Fig. 10. The first observation is that, generally, n-type SnSe has larger values of PFs than p-type SnSe; thus, heavily doped n-type SnSe can exhibit even better thermoelectric performance and better polycrystalline zT over the broad temperature range. It seems that the existence of the structural phase transition is beneficial for the power factor value only for p-type SnSe, where the HT phase exhibits the largest values, but only for large carrier concentrations, for which the bipolar effects are not so important. However, at higher concentrations, the zT value may not benefit from the phase transition because of the increasing contribution of the electronic part of the thermal conductivity.

The maps of PFs also reveal that SnSe is best suited for TE application at temperatures $T > 600$ K and should be rather heavily doped for both n- and p-type SnSe above 10^{20} cm^{-3}.

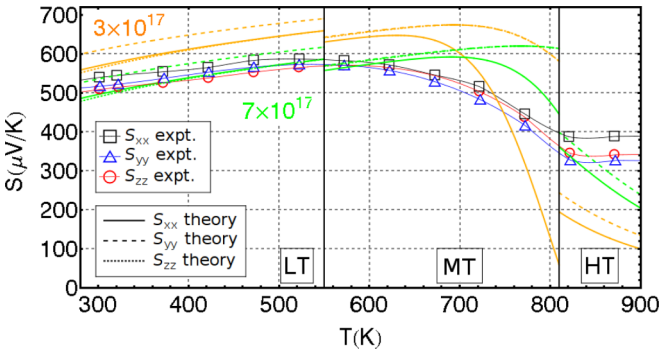

FIG. 11. (Color online) Comparison of the calculated and experimental values [5] of the thermopower vs temperature. Nominal hole concentrations for the theoretical curves are 3×10^{17} (orange) and 7×10^{17} cm^{-3} (green).

Note that all the presented transport calculation results and predictions are based on the constant-relaxation-time approximation, and, in principle, electron-phonon or electron-impurity scattering may markedly affect them. Especially for the case in which both heavy and light electrons are involved in electrical transport, scattering effects may be of increased importance due to the different scattering rates for these two electronic bands.

C. Comparison with experiment

Experimental data were taken from Ref. [5], where the transport properties of the single-crystal p-type SnSe were reported. Since our calculations were performed within the constant-relaxation-time approximation, only thermopower can be directly compared. Figure 11 shows the measured Seebeck coefficient along the a, b, and c crystallographic directions [30] compared with two sets of corresponding theoretical values for hole concentrations $p = 3 \times 10^{17}$ and 7×10^{17} cm^{-3}. These carrier concentrations were selected for comparison based on the measured Hall coefficient of SnSe at $T = 300$ K, which is also depicted in Fig. 12(a). Nevertheless, one has to bear in mind that due to the anisotropic crystal structure and Fermi surface, as well as the strongly nonparabolic band structure, Hall coefficient data do not directly reflect the carrier concentration. In Fig. 11 we see that the experimental Seebeck coefficient matches the theoretical values below 600 K well for $p = 7 \times 10^{17}$ cm^{-3} and then is underestimated in the middle-temperature range (∼700 K). The most intriguing experimental behavior is noticed for the thermopower, which remains constant with temperature above T_c. For such high temperatures and a carrier concentration around $p \sim 10^{17}$ cm^{-3}, the bipolar effect should strongly decrease S, even making S negative, as seen from our computations shown in Figs. 7 and 16. Similar observations with even more quickly decreasing S due to the smaller band gap were reported from calculations in Ref. [9].

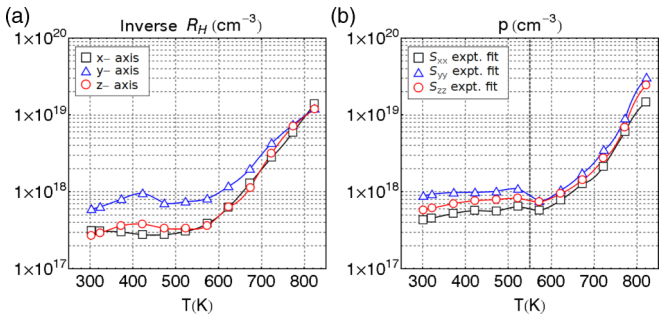

FIG. 12. (Color online) (a) Concentration derived from the measured Hall coefficient, according to $n_H = 1/eR_H$. (b) Nominal carrier concentration at which the calculated thermopower equals the experimental value. All concentrations are given in cm^{-3}, and experimental data are taken from Ref. [5]. Vertical lines separate the temperature ranges, where theoretical thermopower of the LT (below 550 K) and MT (above 550 K) phases was used.

One can attempt to explain such an uncommon situation assuming the gradual increase of the carrier concentration with temperature since it could explain both the decrease in S above 600 K and the saturation of S above 800 K with an almost invisible bipolar effect. Experimental Hall measurements also show that $1/R_H$ increases almost two orders of magnitude [see Fig. 12(a)] between 600 and 800 K, which supports the above-mentioned hypothesis. Moreover, for the high carrier concentration, the thermopower changes smoothly while crossing the phase-transition temperature. Figure 7 shows that only concentrations larger than 1×10^{19} cm^{-3} provide a similar Seebeck coefficient at $T = 807$ K for the MT and HT phases. Finally, measured electrical conductivity (see Ref. [5]) shows nonmonotonic behavior with increasing temperature; that is, it decreases from 300 to 550 K, increases above 550 K, and becomes constant above T_c. Such a trend remains in line with the expectation of increasing carrier concentration above 550 K, where the experimental and theoretical thermopowers start to deviate.

To partly verify this hypothesis, we have plotted how carrier concentration should change with temperature to reach the agreement between the experimental and calculated thermopowers [31]. Carrier concentration p is extracted by applying the condition that $S_{\text{expt.}}(T) = S_{\text{theor.}}(p,T)$ at every T. As we can see in Fig. 12(b), the unusual experimental behavior of thermopower directly results in the increasing carrier concentration in SnSe, to more than 1×10^{19} cm^{-3} around 800 K, and the measured inverse Hall resistivity [Fig. 12(a)] exhibits a temperature dependence similar to that of our extracted $p(T)$ function.

IV. SUMMARY

The electronic structure and thermoelectric properties of n- and p-type SnSe were studied using the KKR method and the Boltzmann transport approach within the constant-relaxation-time approximation. We have shown that the temperature evolution of the crystal structure within the $Pnma$ phase (i.e., before reaching the structural phase transition at 807 K) leads to significant changes in the electronic band structure. On the other hand, the phase transition, occurring at 807 K, leads mainly to the abrupt change in the energy band-gap value, whereas modifications of $\mathscr{E}(\mathbf{k})$ curves are minor. The effective masses, analyzed as a function of the carrier concentration and temperature, indicate that, overall, p-type masses are larger than n-type ones, and SnSe exhibits strong anisotropy

of the electron transport properties for both types of charge conductivity.

Computed for room-temperature crystal structure parameters, p-type SnSe has strongly nonparabolic dispersion relations with a pudding-mold-like shape of the highest valence band. Due to the flat bands yielding large effective masses, the interlayer electron transport seems to be blocked, resulting in small power-factor and Seebeck coefficients when compared with the corresponding values computed for the other directions (i.e., in-plane electron transport).

The opposite situation was found in n-type SnSe, where the interlayer direction exhibits band structure features that are highly beneficial for thermoelectric performance. In this case, when a critical concentration between 10^{19} cm^{-3} (HT) and 10^{20} cm^{-3} (LT; see Fig. 5) is reached or when a high-velocity electron band is thermally activated at high temperatures, two types of carriers are present simultaneously in the system, i.e., more localized electrons, with large effective masses, and highly mobile electrons, which possess low effective masses and high velocity. This particular combination results in high thermopower and a large power factor in the interlayer direction. In view of our results, n-type SnSe may be a better thermoelectric material than p-type SnSe.

Our theoretical study confirmed the strong anisotropy of the electron transport in SnSe. This results in a much worse thermoelectric performance in the polycrystalline material, in agreement with the experimental reports [6,7].

On the whole, the computational results, derived from the KKR method and Boltzmann equations, show quite good agreement with the measured data [5] below $T \sim 600$ K. The experimentally observed changes in S, σ, and R_H for $T > 600$ K suggest that in the measured SnSe samples, the carrier concentration was gradually increasing, and the discrepancy between the theoretical and measured Seebeck coefficients appearing at high temperatures ($T > 600$ K) can be corrected when the actual Hall concentration is taken into account in calculations. Nevertheless, the mechanism responsible for such a generation of additional carriers, suggested in our discussion, remains unknown.

ACKNOWLEDGMENTS

This work was supported by the Polish National Science Center (NCN) under Grant No. DEC-2011/02/A/ST3/00124 and partially by the Polish Ministry of Science and Higher Education.

APPENDIX A: POLYCRYSTALLINE RANDOM-GRAIN MODEL

In a polycrystalline material, where grains have different crystalline orientation and are randomly distributed, the effective Seebeck coefficient and the power factor are not simple averages of the single-grain properties. To obtain the correct isotropic values, an appropriate circuit model for thermoelectric generator is built (see Fig. 13).

In the polycrystalline sample it is assumed that the material consists of three types of small grains, each with thermopower S_k ($k = 1,2,3$) and electrical conductivities σ_k (see Fig. 14)

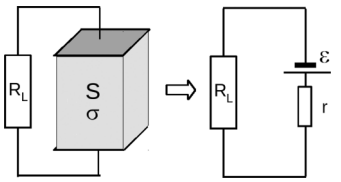

FIG. 13. Circuit model of lumped (with R_L) thermoelectric material.

distributed on a regular grid. This model can be simplified to the thermoelectric module made from three solid materials connected in parallel. On this basis, an equivalent circuit model was made.

The thermoelectric module with one type of material with thermopower S and electrical conductivity σ can be replaced with the electromotive force (emf) $\mathcal{E} = S\Delta T$ and $r = \sigma l/A$, where l and A are the length and cross section of the module, respectively (see Fig. 13). Effective thermopower can be defined as voltage on the module divided by the temperature difference ΔT when R_L goes to infinity.

$$S_{\text{eff}} = \frac{U}{\Delta T} = \frac{iR_L}{\Delta T} = \frac{\mathcal{E}}{r + R_L}\frac{R_L}{\Delta T} \xrightarrow{R_L \to \infty} \frac{\mathcal{E}}{\Delta T} = S, \quad \text{(A1)}$$

where i is the current in the circuit.

The power factor can be defined as the capability of energy production of a material with the cross section A and length l at the given temperature difference ΔT,

$$\text{PF}_{\text{eff}} = \frac{Pl}{A\Delta T^2}, \quad \text{(A2)}$$

where P is the power output of the source when R_L goes to zero (short-circuit power).

$$P = \mathcal{E}i = \frac{\mathcal{E}^2}{r + R_L} \xrightarrow{R_L \to 0} \frac{\mathcal{E}^2}{r}, \quad \text{(A3)}$$

and therefore,

$$\text{PF}_{\text{eff}} = \frac{Pl}{A\Delta T^2} = \left(\frac{\mathcal{E}}{\Delta T}\right)^2 \frac{l}{Ar} = S^2\sigma. \quad \text{(A4)}$$

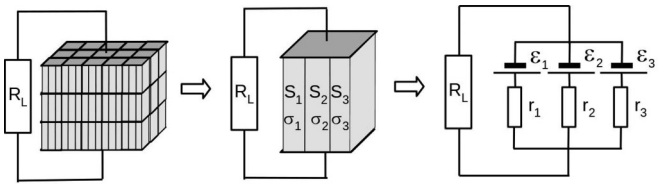

FIG. 14. Model of the thermoelectric material, which is built up from three types of small, randomly distributed grains, with different transport properties.

In the case of the equivalent polycrystalline circuit model, the effective thermopower is

$$S_{\text{eff}} = \frac{U}{\Delta T} = \frac{i R_L}{\Delta T}. \tag{A5}$$

From circuit theory

$$i_k = \frac{\mathcal{E}_k - i R_L}{r_k}, \quad i = \sum_k i_k, \tag{A6}$$

where k is 1,2,3. Now i can be found:

$$i = \frac{\sum_k \mathcal{E}_k / r_k}{R_L \sum_k 1/r_k + 1}. \tag{A7}$$

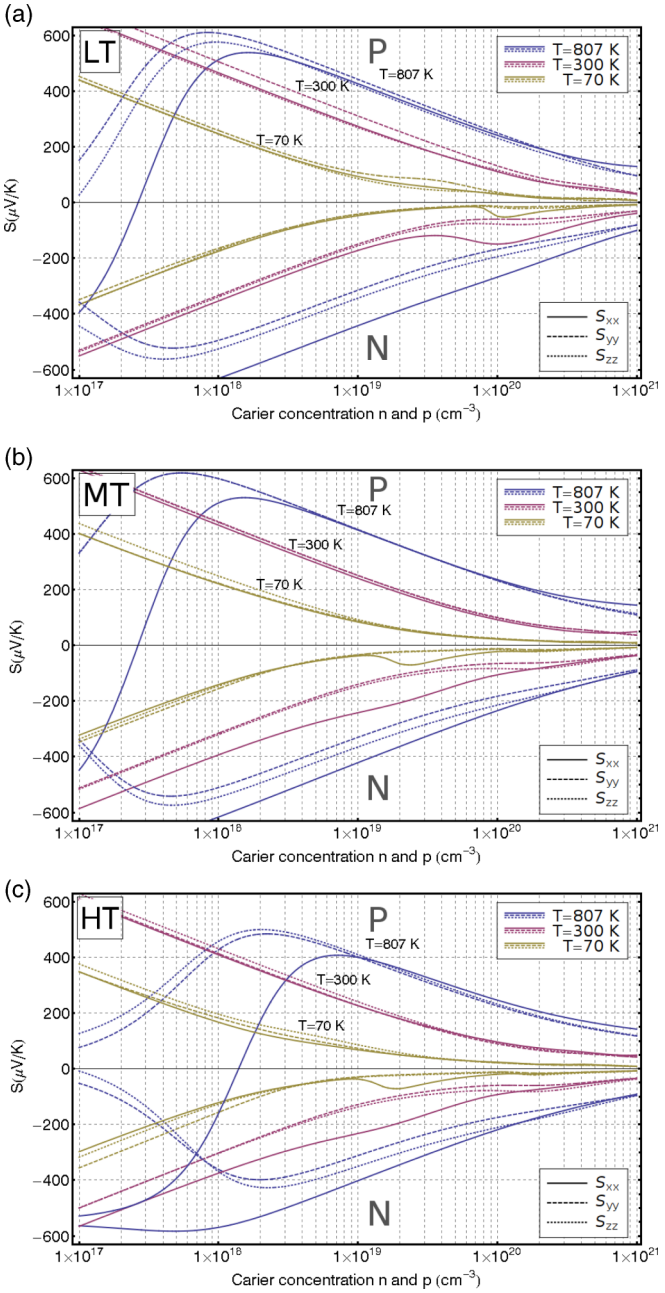

FIG. 15. (Color online) Thermopower (a) LT, (b) MT, and (c) HT phases at three different temperatures and crystallographic directions.

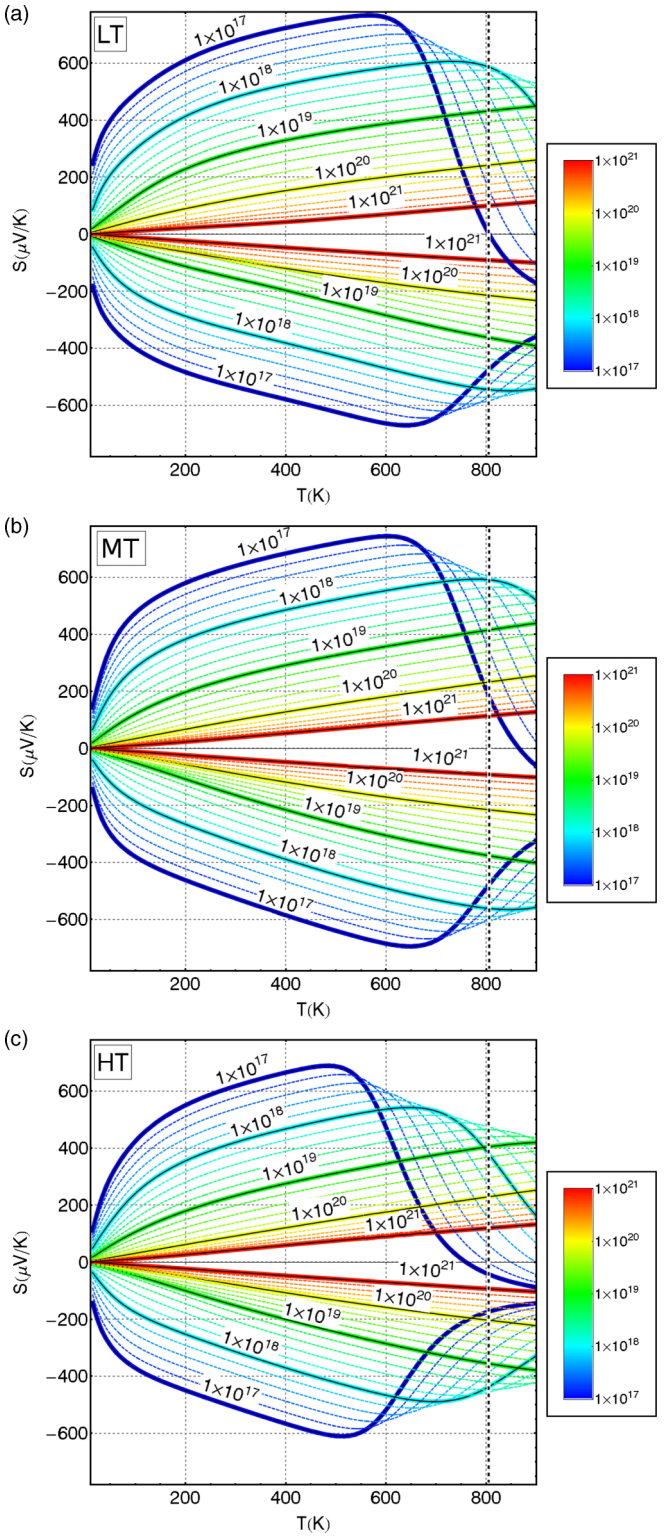

FIG. 16. (Color online) Isotropic thermopower as a function of temperature for (a) LT, (b) MT, and (c) HT for n- and p-type doping. Different colored lines correspond to the different carrier concentrations. Thick lines mark concentrations (in cm^{-3}).

$$S_{\text{eff}} = \frac{iR_L}{\Delta T} = \frac{\sum_k \mathcal{E}_k/r_k}{R_L \sum_k 1/r_k + 1/R_L} \frac{1}{\Delta T} \xrightarrow{R_L\to\infty} \frac{\sum_k \mathcal{E}_k/r_k}{\sum_k 1/r_k} \frac{1}{\Delta T} = \frac{\sum_k S_k\sigma_k}{\sum_k \sigma_k}. \tag{A8}$$

The power of the source is now a sum of powers of all the sources,

$$P = \sum_k \mathcal{E}_k i = \frac{\mathcal{E}_k^2 - i\mathcal{E}_k R_L}{r_k} \xrightarrow{R_L\to 0} \sum_k \frac{\mathcal{E}_k^2}{r_k}, \tag{A9}$$

and therefore,

$$PF_{\text{eff}} = \frac{Pl}{A\Delta T^2} = \sum_k \left(\frac{\mathcal{E}_k}{\Delta T}\right)^2 \frac{l}{A_k r_k} = \frac{1}{3}\sum_k S_k^2\sigma_k, \tag{A10}$$

where $A_k = 1/3A$ (grains are randomly distributed).

APPENDIX B: EXTENDED DATA

This appendix includes additional figures to show the complete data for the anisotropic (Fig. 15) and isotropic (Fig. 16) thermopowers of the three considered SnSe structures.

[1] P. P. Heremans, V. Jovovic, E. S. Toberer, A. Saramat, K. Kurosaki, A. Charoenphakdee, S. Yamanaka, and G. J. Snyder, Science **321**, 554 (2008).

[2] Y. Pei, X. Shi, A. LaLonde, H. Wang, L. Chen, and G. J. Snyder, Nature (London) **473**, 66 (2011).

[3] P. Dziawa, B. J. Kowalski, K. Dybko, R. Buczko, A. Szczerbakow, M. Szot, E. Łusakowska, T. Balasubramanian, B. M. Wojek, M. H. Berntsen, O. Tjernberg, and T. Story, Nat. Mater. **11**, 1023 (2012).

[4] D.-X. Qu, Y. S. Hor, J. Xiong, R. J. Cava, and N. P. Ong, Science **329**, 821 (2010).

[5] L.-D. Zhao, S.-H. Lo, Y. Zhang, H. Sun, G. Tan, C. Uher, C. Wolverton, V. P. Dravid, and M. G. Kanatzidis, Nature (London) **508**, 373 (2014).

[6] S. Sassi, C. Candolfi, J.-B. Vaney, V. Ohorodniichuk, P. Masschelein, A. Dauscher, and B. Lenoir, Appl. Phys. Lett. **104**, 212105 (2014).

[7] C.-L. Chen, H. Wang, Y.-Y. Chen, T. Daya, and G. J. Snyder, J. Mater. Chem. A **2**, 11171 (2014).

[8] T. Chattopadhyay, J. Pannetier, and H. G. Von Schnering, J. Phys. Chem. Solids **47**, 879 (1986).

[9] G. Shi and E. Kioupakis, J. Appl. Phys. **117**, 065103 (2015).

[10] N. W. Ashcroft and N. D. Mermin, *Solid State Physics* (Harcourt College Publishers, Orlando, 1976).

[11] T. Thonhauser, T. J. Scheidemantel, J. O. Sofo, J. V. Badding, and G. D. Mahan, Phys. Rev. B **68**, 085201 (2003).

[12] G. K. H. Madsen, K. Schwarz, P. Blaha, and D. J. Singh, Phys. Rev. B **68**, 125212 (2003).

[13] K. Kutorasinski, J. Tobola, and S. Kaprzyk, Phys. Rev. B **87**, 195205 (2013).

[14] L. Chaput, P. Pecheur, J. Tobola, and H. Scherrer, Phys. Rev. B **72**, 085126 (2005).

[15] K. Kutorasinski, B. Wiendlocha, J. Tobola, and S. Kaprzyk, Phys. Rev. B **89**, 115205 (2014).

[16] E. A. Stern, Phys. Rev. **157**, 544 (1967).

[17] H. Kohn and N. Rostoker, Phys. Rev. **94**, 1111 (1954).

[18] W. H. Butler, Phys. Rev. B **14**, 468 (1976).

[19] S. Kaprzyk and A. Bansil, Phys. Rev. B **26**, 367 (1982).

[20] S. Kaprzyk and A. Bansil, Phys. Rev. B **42**, 7358 (1990).

[21] A. Bansil, S. Kaprzyk, P. E. Mijnarends, and J. Tobola, Phys. Rev. B **60**, 13396 (1999).

[22] T. Stopa, S. Kaprzyk, and J. Tobola, J. Phys. Condens. Matter **16**, 4921 (2004).

[23] D. D. Koelling and B. N. Harmon, J. Phys. C **10**, 3107 (1977).

[24] H. Ebert, H. Freyer, and M. Deng, Phys. Rev. B **56**, 9454 (1997).

[25] J. P. Perdew and Y. Wang, Phys. Rev. B **45**, 13244 (1992).

[26] W. E. Lorensen and H. E. Cline, Comput. Graphics **21**, 163 (1987).

[27] H. Gouraud, IEEE Trans. Comput. **100**, 623 (1971).

[28] We use the term *phase* to name the three different crystal unit cells of SnSe, even if, in fact, LT and MT have the same space group and so are not exactly different crystalline phases.

[29] K. Kuroki and R. Arita, J. Phys. Soc. Jpn. **76**, 083707 (2007).

[30] The original data from Ref. [5] were transformed to our convention of the unit-cell axes. In Ref. [5] axis c is the shortest one; thus, b and c are exchanged compared to our convention of $Pnma$.

[31] Carrier concentration p is extracted by applying the condition that $S_{\text{expt.}}(T) = S_{\text{theor.}}(p,T)$ at every T.